

Stabilizing Particles of Manganese-iron Oxide with Additives for Thermochemical Energy Storage

N. C. Preisner,^{*,[a]} T. Block,^[b] M. Linder,^[a] and H. Leion^[c]

Manganese-iron oxide particles are a promising candidate for both chemical-looping combustion (CLC) and thermochemical energy storage. In CLC, the ability of metal oxides to oxidize fuels in an oxygen-free atmosphere and re-oxidize in air is addressed. Whereas, reaction enthalpy is the main focus of thermochemical energy storage for, e.g. concentrated solar power or an industrial process that requires high temperature levels. Sufficient mechanical strength of the particles while they endure chemical, thermal, or mechanical stress is a crucial factor for both concepts. Particle stability is investigated here by adding 20 wt.% of TiO_2 , ZrO_2 , or CeO_2 as a supportive material to $(\text{Mn}_{0.7}\text{Fe}_{0.3})_2\text{O}_3$. Thermal cyclization and temperature shock tests are conducted in a packed bed

reactor to identify chemical stability as well as the effect of chemical and thermal stress. A subsequent particle size distribution analysis is performed to determine the relevant breakage mechanism. Attrition resistance is tested with a customized attrition jet cup to estimate the mechanical strength of particles. It is found that the high tendency of unsupported manganese-iron oxide particles towards agglomeration can be improved with any of the chosen additives. The particles with CeO_2 , and especially with ZrO_2 , as an additive indicate an increase in resistance towards attrition. However, adding TiO_2 has a severe negative impact on the chemical reactivity of the manganese-iron oxide.

Introduction

The characteristic redox reaction of metal oxides is applied in several research fields, which are motivated by the necessity to mitigate global warming. Metal oxides are currently investigated for example as thermochemical energy storage material, for solar fuel production, and for chemical looping combustion. All of these applications utilize metal oxides in the form of particles and thus rely on a sufficient stability of the particles. Chemical looping combustion (CLC) is based on the ability of metal oxides (oxygen carriers) to oxidize in a reactor with air and carry oxygen to a fuel reactor, where the metal oxides react with gas-phase combustibles.^[1] In chemical looping with oxygen uncoupling (CLOU), the metal oxide releases gaseous oxygen in the fuel reactor, which is needed to oxidize not only the gas phase but also liquid and solid fuels.^[2] The exhaust gas of the fuel reactor consists of CO_2 and H_2O , which can be easily separated. The only exhaust from the air reactor is depleted air. Usually the concept is implemented in the form of two interconnected fluidized beds to allow a continuous operation with biomass, coal, methane, or any other fuel. Reactor setups are tested that range from lab-scale units,^[3,4] a 100 kW_{th} unit at Chalmers in Sweden,^[5] to a 1 MW_{th} pilot plant at TU Darmstadt, Germany.^[6] Recent promising metal oxide candidates are perovskites^[7] and Mn-combined oxides, e.g. manganese-iron oxides.^[8] Natural ores are successfully tested.^[9] Another application of metal oxides is the production of solar fuels, namely H_2 and CO , by splitting H_2O and CO_2 with metal oxides.^[10] The produced syngas can be further processed to denser liquid fuels via the Fischer-Tropsch process. The high temperature needed for reducing metal oxides in air is supplied by renewable sources, e.g. a concentrating solar power plant. Implemented reactor

concepts focus on porous structured metal oxides^[11] in a rotary kiln,^[12] moving particles in a fluidized bed reactor,^[13] a cavity reactor,^[14] a moving bed reactor,^[15–17] and a packed bed reactor.^[18–20]

Sustainable fuel conversion is the main objective of chemical looping and solar fuel research. However, the reaction enthalpy of the redox reaction is the main objective of thermochemical energy storage research. Thermochemical storage (TCS) systems are a promising way to increase the flexibility of concentrated solar power plants (CSP) or industrial processes operated at high temperature (700–1000 °C).^[21–26] Especially weather instability and expandable operation time can be addressed with TCS systems to lower the cost of CSP and provide dispatchable power generation.^[27] The reaction enthalpy of a chemical reversible gas-solid reaction stores heat in the endothermic reaction path and releases heat in the exothermic path. Solid gas redox reactions of metal oxides in air are suitable candidates for exploiting the accessible high temperatures of CSP. Besides applicable reaction temperature, the metal oxide should feature suffi-

[a] N. C. Preisner, Dr. M. Linder
Thermal Process Technology
DLR, Institute of Engineering Thermodynamics
Linder Höhe, 51147 Köln, Germany
E-mail: Nicole.Preisner@dlr.de

[b] Dr. T. Block
Structural and Functional Ceramics
DLR, Institute of Material Research
Linder Höhe, 51147 Köln, Germany

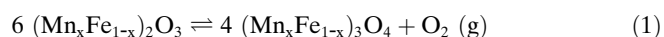
[c] Dr. H. Leion
Chemistry and Chemical Engineering
Chalmers University of Technology
Kemigården 4, Göteborg, Sweden

Supporting information for this article is available on the WWW under <https://doi.org/10.1002/ente.201800211>

cient mechanical strength, fast kinetics, high reaction enthalpy, and cycle stability.

Since oxygen from ambient air can be used as the reaction gas for a thermochemical reaction, no separate gaseous storage is necessary. The concept of two interconnected reactors for continuous charging and discharging is presented by Schrader et al.^[28] with CoO as thermochemical storage material and heat transfer medium. A solar reactor for reduction and an oxidation reactor are combined with cold and hot storage tanks to feed an air Brayton cycle. For this reason, the storage capacity and power are decoupled, allowing the separate adjustment of both power and capacity. In these continuous reactors, it is possible to extract thermochemical and sensible thermal energy and, thus, increase the energy density of metal oxide particles. So far, solar receivers for the reduction of metal oxide particles by direct solar radiation apply rotary kiln,^[29,30] gravity-driven particle receivers^[31,32] or packed bed reactors.^[33] A fluidized bed reactor^[35] and packed bed reactors^[25,34] were investigated for reactors that are able to oxidize metal oxide particles and extract heat to a working fluid. A further development of the packed bed to a moving bed as a reactor concept for continuous heat extraction combines two main advantages. First, thermochemical as well as sensible heat can be extracted from the metal oxide particles to improve overall efficiency, while a stable temperature of a working fluid is allowed. Second, no moving reactor components at high temperatures need to be handled since particles are transported by gravity in contrast to continuous reactors like rotary kiln or sintering bands.

Manganese-iron oxides have an equilibrium temperature in air atmosphere between 900 °C and 1400 °C, depending on the manganese-to-iron ratio. Thermodynamic investigations of the manganese-iron-oxygen system in air identify the cubic bixbyite phase $[(\text{Fe}^{3+}, \text{Mn}^{3+})_2\text{O}_3]$, and the trigonal hematite phase (Fe_2O_3) at low temperatures and the cubic spinel phase $[(\text{Fe}^{2+}, \text{Mn}^{2+})(\text{Fe}^{3+}, \text{Mn}^{3+})_2\text{O}_4]$, and tetragonal hausmannite phase $[(\text{Mn}^{2+})(\text{Mn}^{3+})_2\text{O}_4]$ at high temperatures as thermodynamically stable phases.^[36–39] The oxides are non-toxic and show acceptable reaction time for oxidation and reduction as well as cycle stability. Several studies have investigated the redox behavior of manganese-iron-oxide systems with different manganese-iron ratios for thermochemical applications.^[22,40–42] Equation (1) presents the global reaction of manganese-iron oxides between bixbyite and spinel, which can be initiated by changing oxygen partial pressure or/and temperature.



A stoichiometric weight change caused by the redox reaction of 3.340 to 3.378 % with the Mn-cation content $(\text{Mn}/(\text{Mn} + \text{Fe})) \times$ between 0 and 1 can theoretically be achieved. However, agglomeration and particle stability problems occur after a number of redox reactions of $(\text{Mn}_{0.75}\text{Fe}_{0.25})_2\text{O}_3$ granules in a packed bed reactor.^[34] Under chemical looping conditions, similar problems with manganese-iron-oxide particles in

a fluidized bed reactor have been reported.^[43] A reactor concept with moving particles, such as a reactor with a moving bed or a fluidized bed, induces even greater stress on the particles than a packed bed. The attrition of particles results in the loss of material when small particles must be removed and a recycling or filtration system becomes necessary. Moreover, decreasing particle size causes higher pressure losses and, thus, lowers the performance of a reactor setup.

Particles undergo several kinds of stress in a reactor, such as chemical, mechanical, and thermal stress. As a consequence, particles may split, become fatigued, fractures may spall, or the surface may be smoothed due to attrition or abrasion, leading to a shift in particle size distribution. Mechanical stress includes particle-wall or particle-particle collision. When the kinetic energy of a collision at high velocity is absorbed, particles may fracture or be abraded. A low velocity collision causes surface abrasion resulting in very fine particles by smoothing the small edges on the particle. Particles endure thermal stress in the form of high heating or cooling rates, temperature gradients inside the particle, or different thermal expansion coefficients of multiphase particles.^[44] Chemical reactions can cause stress when phases with different densities or molar volumes are formed, resulting in intraparticle stresses, e.g. the reduction of Fe_2O_3 caused by the expansion of ferrite oxide crystals.^[45] A change in pore structure may weaken the overall particle,^[46] and the release of gas during a reaction can cause an internal pressure gradient in gas-solid reactions.

The agglomeration tendency of particles is an important criterion for the expected useful lifetime of any thermochemical storage material. Agglomeration can be caused by a temperature exceeding the onset sinter temperature, chemical reactions, or particle-collision-induced melting.^[45,47,48] Since any change in particle size distribution may have a tremendous impact on reactor performance, possibilities to improve the particle stability of chemically reacting Manganese-iron oxides are addressed in this paper.

Particle strength can be improved by adjustments made in the particle preparation, for instance, by choosing sol-gel granulation, spray drying, using precipitation methods, or by adding binders. Coating with a strong porous material can also strengthen particles as well as introducing compressive stresses by rapid heating and cooling of particles to harden the particle surface without sintering or phase changes.^[44]

The fluidized bed concept utilized in CLC can cause the severe attrition of oxygen carrier particles. Thus, in the research field of chemical looping, great effort has been put into improving, measuring, and predicting the strength of metal oxide particles and their agglomeration tendency.^[50] Adding supportive inert material, optimizing the calcination temperature, or choosing an adapted preparation method have shown promising results. Azimi et al.^[51] have investigated the effect of different additives (40 wt.%) to spray-dried $(\text{Mn}_{0.75}\text{Fe}_{0.25})_2\text{O}_3$ particles on mechanical strength and reactivity under chemical-looping conditions. Attrition resistance was found to be substantially improved with the addition of ZrO_2 (monoclinic), depending on the calcination temper-

ature of the particles. For this reason, the use of a rather low calcination temperature is recommended.^[51] A fixed amount of 7 wt.% TiO_2 was added by the authors of^[52] for its reactivity and magnetic properties to manganese-iron oxides with a Mn:Fe ratio between 0 and 1 and under chemical looping conditions. An increase in crushing strength was found compared to particles without the addition of Ti.

Particle stability and the modification of metal oxides have been comprehensively investigated by the chemical-looping research community.^[46,53–55] However, operation conditions and applied reactor concepts differ between chemical-looping and thermochemical storage applications. In CLC, isothermal reaction conditions are mainly applied in O_2 depleted air for the oxidation of metal oxides, and a fuel atmosphere for the reduction of metal oxides.^[2] In contrast, in the thermochemical storage concept, the reduction in O_2 -depleted air and oxidation in air are initiated thermally by exceeding the equilibrium temperature or by changing the partial pressure of O_2 under isothermal conditions.^[34] Particle size may vary depending on the applied reactor concept. For these reasons, it remains uncertain if the findings from particle stability investigations under chemical-looping conditions can be applied to thermochemical storage applications. This paper presents an investigation of the effect of the addition of ZrO_2 , CeO_2 , or TiO_2 to manganese-iron oxide on reactivity, agglomeration, and attrition behavior under the specific conditions relevant for thermochemical storage using a moving bed reactor.

Results and Discussion

Characterisation of the Material

A manganese-iron oxide with a Mn/Mn+Fe ratio of 0.7 was chosen as a promising thermochemical storage material due to its suitable redox reaction time and temperature, cycle stability and reaction enthalpy.^[22,41,42] To further improve the mechanical strength of the material, ZrO_2 , CeO_2 , or TiO_2 was added as a support, each equaling 20 wt.% of the particle composition. Detailed composition and material properties are given in Table 1. The composition specifies the weight fraction of raw materials used for producing the particles.

Scanning electron microscopy was used to characterize the microstructures of all untreated samples (Figure 1). Internal imperfections are visible in the polished microsections in the figure. Further investigation with EDX indicated iron-rich, manganese-rich, and additive-rich regions. A bimodal grain distribution with larger Fe-rich regions and smaller Mn-rich regions was identified in the $(\text{Mn}_{0.7}\text{Fe}_{0.3})_2\text{O}_3$ particles. The internal distribution of the additive material seemed to increase in heterogeneity from Zr-cation, Ti-cation, to Ce-cation. Detailed data can be found as supporting information.

Table 1. Composition and bulk density of manganese-iron-oxide materials.

Acronym ^[a]	Molar Composition	Composition of raw materials (wt.%)	Bulk density (kg m^{-3})
Mn70Fe30	$(\text{Mn}_{0.7}\text{Fe}_{0.3})_2\text{O}_3$	69 % Mn_2O_3 31 % Fe_2O_3	1330
Mn70Fe30_Zr20	$(\text{Mn}_{0.7}\text{Fe}_{0.3})_2\text{O}_3/\text{ZrO}_2$	55.2 % Mn_2O_3 24.8 % Fe_2O_3 20 % ZrO_2	1539
Mn70Fe30_Ce20	$(\text{Mn}_{0.7}\text{Fe}_{0.3})_2\text{O}_3/\text{CeO}_2$	55.2 % Mn_2O_3 24.8 % Fe_2O_3 20 % CeO_2	1366
Mn70Fe30_Ti20	$(\text{Mn}_{0.7}\text{Fe}_{0.3})_2\text{O}_3/\text{TiO}_2$	55.2 % Mn_2O_3 24.8 % Fe_2O_3 20 % TiO_2	1193

[a] The acronym describes the molar ratio of Mn and Fe cations and the weight fraction of added ZrO_2 , TiO_2 , or CeO_2 .

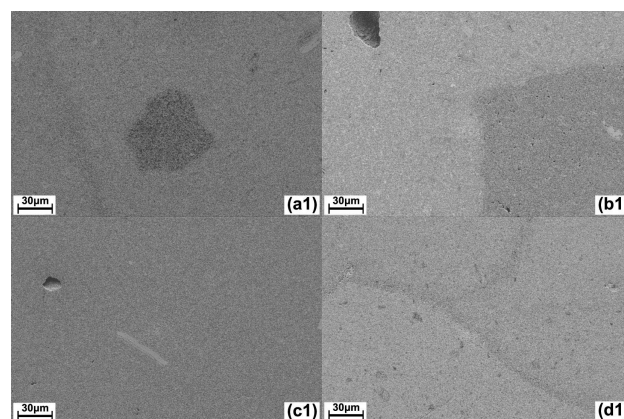


Figure 1. SEM profile image with 5.0 kV acceleration voltage and working distances of 8.0 mm (a, c, d) and 7.9 mm (b) of untreated Mn70Fe30 (a1), Mn70Fe30_Ce20 (b1), Mn70Fe30_Ti20 (c1), and Mn70Fe30_Zr20 (d1).

Effect of Additives on Energy Storage Density

A modification with inert additives potentially lowers the total energy density, since inert additives do not contribute to the thermochemical share in energy density. Regarding the sensible thermal energy stored in the particles, a supportive material with high heat capacity should be favored in case of thermochemical energy storage application, whereas a lower heat capacity is beneficial in case of CLC application. Rutile (TiO_2) offers the highest mean heat capacity of $934.04 \text{ J kg}^{-1} \text{ K}^{-1}$ for temperatures between 600 K and 1300 K, followed by ceria (CeO_2) with $603.56 \text{ J kg}^{-1} \text{ K}^{-1}$ and zirconia (ZrO_2) featuring $450.24 \text{ J kg}^{-1} \text{ K}^{-1}$.^[56] However, the bulk density of manganese-iron oxides with the addition of ZrO_2 is slightly higher than with the addition of TiO_2 , which affects the volumetric energy density of the storage material. When inert, the support material does not contribute to the thermochemical share of energy density.

According to reaction equation (1), a stoichiometric mass loss of 3.366 % can be calculated for pure $(\text{Mn}_{0.7}\text{Fe}_{0.3})_2\text{O}_3$. The additive, when behaving inert, reduces the stoichiometric mass loss to 2.693 % for $(\text{Mn}_{0.7}\text{Fe}_{0.3})_2\text{O}_3$ with 20 wt.% of ZrO_2 ,

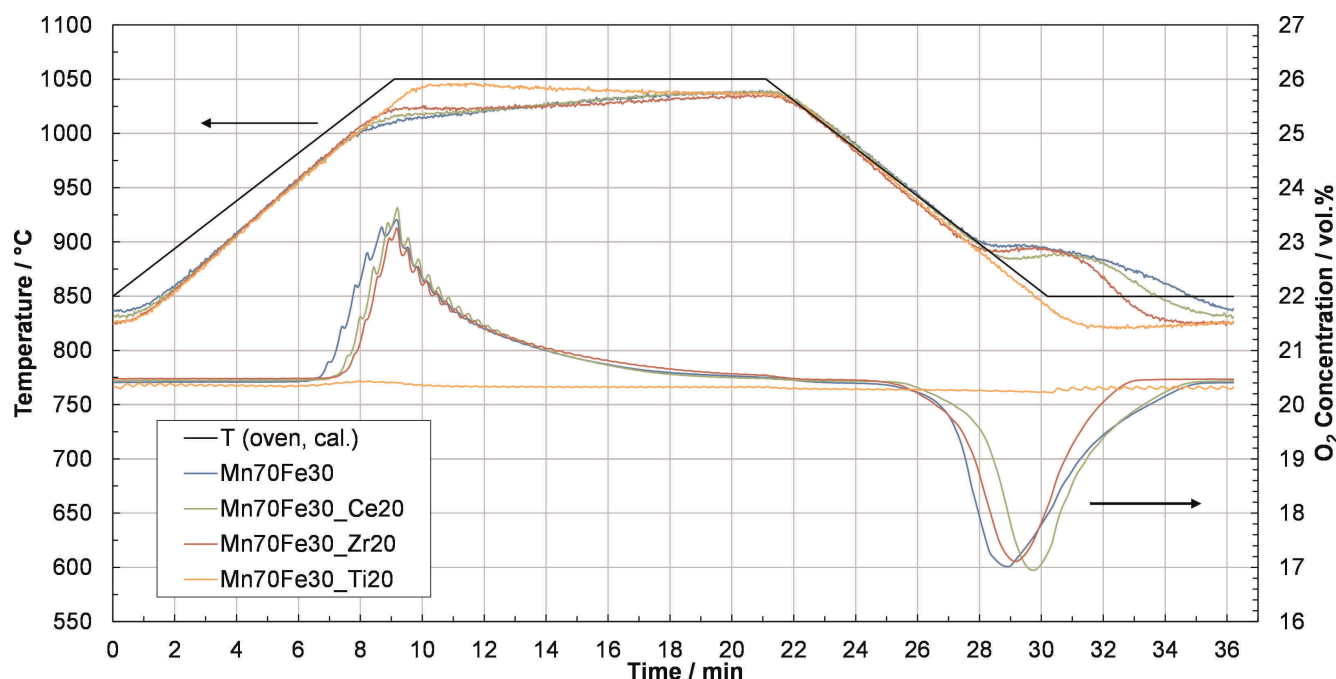


Figure 2. Measured bed temperature and set point temperature of the 25th cycle (upper curves) and O₂ concentration (lower curves) of 25th cycle of thermal cyclization in lab-scale packed bed reactor with pure (Mn_{0.7}Fe_{0.3})₂O₃ or supported with TiO₂, ZrO₂, or CeO₂.

TiO₂, or CeO₂. Thermogravimetric measurements with Mn70Fe30, Mn70Fe30_Zr20, or Mn70Fe30_Ce20 confirmed the stoichiometric mass loss of equation (1) with a deviation of 0.04–0.06 wt.%. Whereas Mn70Fe30_Ti20 showed a higher mass loss during reduction than pure Mn70Fe30, indicating that equation (1) is not the predominant reduction reaction under the given conditions.

Effect of Thermal Cyclization

The effects of chemical and thermal stress on supported manganese-iron oxide particles were investigated and quantified in the study. The experiments were conducted in a packed bed reactor to inhibit any friction of the material.

The effect of chemical stress on the particle stability and the reactivity of pure manganese-iron oxide and manganese-iron oxide with the addition of CeO₂, ZrO₂, or TiO₂ were investigated with thermal cyclization tests. The reduction and oxidation was initiated by changing the set point temperature of the oven between 850 °C and 1050 °C for 30 cycles.

The ability of manganese-iron oxides with different supporting additives to perform reversible redox reactions in air is illustrated in Figure 2 with the exemplary 25th cycle. An increase in O₂ concentration denotes the reduction to (Mn_{0.7}Fe_{0.3})₃O₄, and a decrease in O₂ concentration denotes the oxidation to (Mn_{0.7}Fe_{0.3})₂O₃ for Mn70Fe30 according to equation (1). The O₂ concentration in the exhaust gas of Mn70Fe30_Ti20 during thermal cyclization indicated no relevant reduction or oxidation of the material, whereas pure (Mn_{0.7}Fe_{0.3})₂O₃ and the samples supported with CeO₂ and

ZrO₂ were reduced and oxidized in air atmosphere. The increase in O₂ concentration up to a peak of around 23.5 % or reduction down to around 17 % was similar for the three remaining compositions, but varied in time and in temperature. The area under the O₂ line correlates to the extent of conversion. During the reduction of the 25th cycle, Mn70Fe30 reached the highest reduction conversion, even though the reactive mass was identical for the three samples. A detailed analysis of the oxidation conversion is given in Figure 3. The endothermic reduction started at around 971 °C, which limited the bed temperature during heating and the subsequent isothermal phase. The initiation temperature of reduction, however, seemed to decrease between Mn70Fe30_Zr20, Mn70Fe30_Ce20 to Mn70Fe30. The exothermic oxidation began slowly at around 966 °C and led to a temperature plateau in the range of 895 °C for Mn70Fe30 and Mn70Fe30_Zr20 and around 889 °C for Mn70Fe30_Ce20 during the cooling phase. The initiation temperatures of reduction and oxidation of Mn70Fe30 and Mn70Fe30_Ce20 were stable during 30 temperature cycles and were in agreement with reported equilibrium temperatures in phase diagrams.^[36,37,39] The initiation temperature of reduction and oxidation of Mn70Fe30_Zr20 showed a slight increase during cyclization from 975 °C to 983 °C in case of reduction and from 960 °C to 972 °C in case of oxidation. The conversion presented in Figure 3 was calculated as oxygen loss in the gas stream due to the oxidation of the particles relative to the stoichiometric oxygen uptake of the active manganese-iron oxide content, for the 2nd and last performed oxidations.

Only 28 cycles could be performed for Mn70Fe30_Zr20 due to practical reasons, while 30 cycles were conducted with

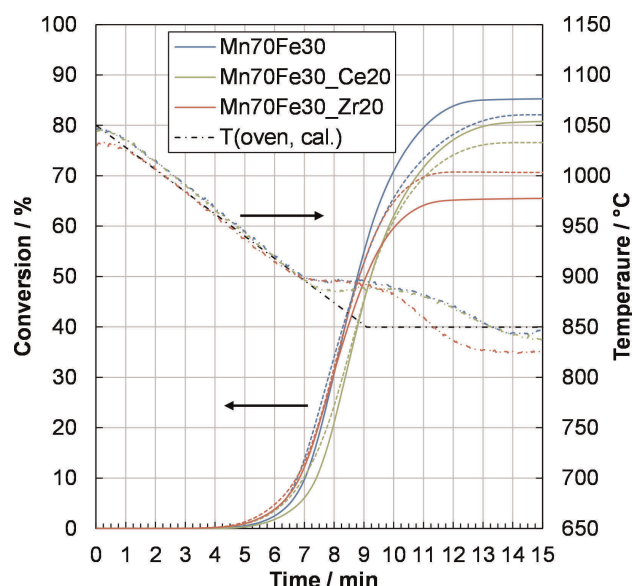


Figure 3. Oxidation conversion of Mn70Fe30 (blue), Mn70Fe30_Ce20 (green), and Mn70Fe30_Zr20 (red), relative to the stoichiometric oxygen uptake of the active manganese-iron oxide content in the sample, during the 2nd (—) and 28th (---) (Mn70Fe30_Zr20) or 30th (---) cycle of thermal cyclization in a packed bed reactor. The bed temperature (—•—) is displayed for the 2nd cycle of each composition as well as the set point temperature of the kiln.

the other displayed compositions. Each sample has been cooled to ambient temperature in air between the two displayed cycles, because the cyclization was performed on two consecutive days. The given time started at the end of the isothermal step at 1050°C. No conversion calculations were performed for Mn70Fe30_Ti20 since the O₂ concentration in the exhaust gas indicated only minor reduction and oxidation after one reduction during the first cycle. A detailed depiction of the occurring phases is presented in Figure 8–11. The manganese-iron oxides with the addition of CeO₂ and ZrO₂ showed a lower conversion than Mn70Fe30. While 85.2 % of the pure Mn70Fe30 sample could be oxidized during the 2nd cycle, Mn70Fe30_Ce20 and Mn70Fe30_Zr20 reached a total conversion of 80.8 % and 65.5 %, respectively. The length of the temperature plateaus in Figure 3 reflects the discrepancy between achieved conversion values, and the plateau formation is directly related to the highest oxidation rate. The conversion trend of Mn70Fe30 and Mn70Fe30_Ce20 declined with increasing cyclization number and showed no continuous effect of the prolonged oxidizing conditions while the reactor was cooled to ambient temperature after one day of experiments. In contrast, the cooling-down phase of a Mn70Fe30_Zr20 packed bed significantly improved the conversion of the redox reaction, resulting in an increase in conversion for the 28th cycle of 70.75 %. Furthermore, the reaction time needed to achieve 0.1 % to 50 % conversion increased for Mn70Fe30 and Mn70Fe30_Ce20 from the 2nd to the 30th cycle. Up to this point, Mn70Fe30 and Mn70Fe30_Ce20 seemed to be the most promising candidates as energy storage material with respect to oxidation behavior. It should be noted that the oxidation conversion of Mn70Fe30_Zr20 benefited most of the pro-

longed oxidation during the cooling of the packed bed between day 1 and 2. For this reason, a longer isothermal step may improve the cycle stability.

To eliminate the influence of the experimental conditions on the conversion results, the mass loss during 30 cycles of each material was measured with a simultaneous thermal analyzer. The temperature profile and the gas atmosphere was adjusted according to thermal cyclization conditions. The conversion of the 2nd, 15th, and 30th cycle was normalized with the stoichiometric mass loss (Table 2). After a mass loss of

Table 2. Conversion stability of pure and supported manganese-iron-oxide particles. 30 Cycles were performed with a simultaneous thermal analyzer with conditions similar to thermal cyclization experiments in a packed bed reactor.

Material	Cycle 2 Red.	Ox.	Cycle 15 Red.	Ox.	Cycle 30 Red.	Ox.
Mn70Fe30	92.4 %	91.5 %	92.1 %	91.8 %	92.4 %	91.2 %
Mn70Fe30_Zr20	92.8 %	92.1 %	91.3 %	91.7 %	92.1 %	91.3 %
Mn70Fe30_Ce20	92.1 %	92.1 %	91.7 %	91.4 %	91.4 %	89.9 %

1.40 % during the first reduction of Mn70Fe30_Ti20, only minor mass changes were observed in subsequent cycles. All materials, except Mn70Fe30_Ti20, showed stable conversion rates over 30 cycles with thermal cyclization conditions.

A particle size distribution analysis can reveal the predominant breakage mechanism. Therefore, the distribution before and after a treatment that caused stress to the particles was compared.^[58] In the differential particle size distribution plot (Figure 4), positive weight fractions denote an increase in the weight fraction for the given particle size, whereas a negative value corresponds to a decrease in the weight fraction for the given particle size. All samples were treated in a vibrating machine for 10 minutes to separate the different particle sizes according to the mesh sizes of the sieves.

The particle size distribution of untreated Mn70Fe30_Ce20 is included to illustrate the original particle size distribution of all the tested materials, which showed a very similar distribution. The Mn70Fe30 sample showed a high tendency towards agglomeration as indicated by particle sizes above the original 2–3 mm. In addition, the disintegration mechanism led to the production of fines for Mn70Fe30 after 30 cycles, which is displayed enlarged in the right corner. An image of a Mn70Fe30 agglomerate and Mn70Fe30 fines is presented in Figure 5 and Figure 6, respectively. The bed volume of Mn70Fe30 particles increased by 17 %, which could represent a particle “swelling” and result in an increased amount of particles in the diameter range of 3–4 mm. Wokon et al.^[42] have reported a similar effect for (Mn_{0.75}Fe_{0.25})₂O₃ particles in the size range of 1–3 mm after 100 redox cycles. In addition, Brown et al.^[46] have described an increase in the swelling effect for pure iron oxide particles, when they performed continuing redox reactions between Fe₂O₃ and Fe₃O₄ phase. The authors identified the formation of a porous instead of a lamella magnetite as the crucial point, and this

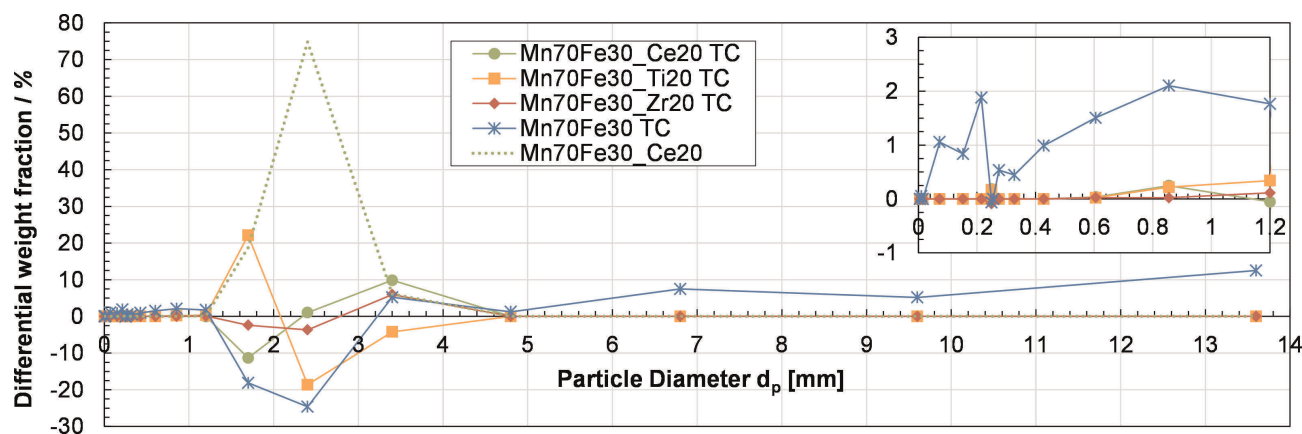


Figure 4. Differential particle size distribution of pure $(\text{Mn}_{0.7}\text{Fe}_{0.3})_2\text{O}_3$ and manganese-iron oxide with supporting additives after 30 cycles of thermal cyclization (TC) in a packed bed reactor compared to untreated particle size distribution with a close up of 0 to 1.2 mm particle size in the upper right corner. The values display the difference between the weight fraction of each measured particle size range before and after particle treatment in a packed bed reactor. The green dotted line symbolizes original particle size distribution before any treatment. The plotted particle size was calculated as arithmetic mean particle size of the sieve sizes.



Figure 5. Mn70Fe30 agglomerate after 30 temperature cycles.



Figure 6. Mn70Fe30 bulk after 30 temperature cycles.

resulted in fragile particles with a tendency towards fragmentation. Carrillo et al.^[41] suspect that sintering processes, or more precisely, a complete morphology change caused by high temperature conditions for the reduction and oxidation of $\text{Mn}_2\text{O}_3/\text{Mn}_3\text{O}_4$ or $(\text{Mn},\text{Fe})_2\text{O}_3/(\text{Mn},\text{Fe})_2\text{O}_3$ systems, are responsible for low re-oxidation rates. Those authors present sintering as a combination of densification and coarsening phenomena. They suggest that the sintering process impedes oxygen diffusion through Mn_3O_4 layers because of reduced active surface or particle aggregation.

In contrast to Mn70Fe30, all supported manganese-iron oxides showed no rise in bed volume height after 30 temperature cycles. All the supportive materials obviously impeded the agglomeration phenomenon to a minimum. Mn70Fe30_Ce20 and Mn70Fe30_Zr20 particles showed a redistribution of particle size from the lower end of original particle size to slightly larger particles. Some particles must have agglom-

erated, since no “swelling” effect could be observed. In contrast, Mn70Fe30_Ti20 particles tended towards breakage instead of disintegration and showed no agglomeration phenomenon.

In order to better understand and support the above findings, a detailed analysis of the morphology of the samples was performed. SEM images showed enlarged grains with irregular morphology in a comparison of the particle surface after thermal cyclization of Mn70Fe30, Mn70Fe30_Ti20, Mn70Fe30_Ce20, and Mn70Fe30_Zr20 (Figure 7) with untreated material.

The addition of ZrO_2 in particular seemed to reduce grain growth on particle surface during thermal cyclization (Figure 7 c1-c2). In a comparison of manganese-iron oxide with the addition of CeO_2 , ZrO_2 , or TiO_2 , Mn70Fe30_Ce20 developed the largest and most irregular surface grains and the most agglomerates, which is in agreement with the agglomeration tendency after redox reactions in air, indicated by the differential particle size distribution (Figures 4 and 12a).

XRD analyses of samples after thermal cyclization (Figures 8–11) suggested that ZrO_2 and CeO_2 are mostly inert additives to $(\text{Mn}_{0.7}\text{Fe}_{0.3})_2\text{O}_3$. This is in agreement with Bhavsar et al.^[48] However, the CeO_2 -supported manganese-iron oxide sample was not completely oxidized after thermal cyclization with subsequent cooling to ambient temperature in air. Furthermore, the TiO_2 -supported manganese-iron oxide sample formed an iron-titanate phase, detected as pseudobrookite (Fe_2TiO_5) with XRD, which also detected bixbyite (Mn_2O_3) and hematite (Fe_2O_3). According to Anovitz et al.,^[62] pseudobrookite is formed from hematite (Fe_2O_3) and rutile (TiO_2) and remains stable above 585°C , which explains the poor reactivity of this sample (see Figure 2). Therefore, pseudobrookite could have been already formed during the preparation process of the Mn70Fe30_Ti20 particles.

Thermal cyclization experiments focused mainly on chemical stress, but it must be noted that by initiating the redox

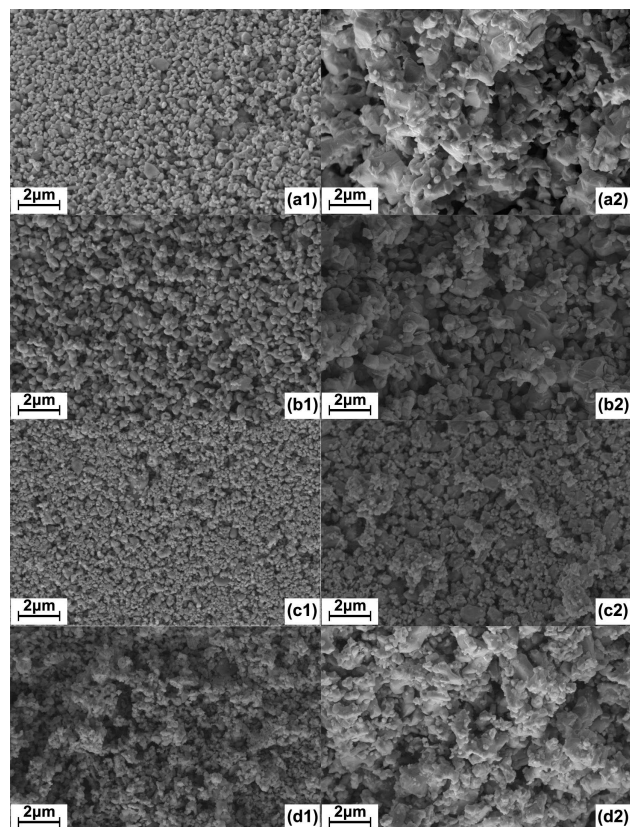


Figure 7. SEM images with 5.0 kV acceleration voltage and working distances 8.0 mm (a1, b1, b2, c1, c2 and d1, d2) and 7.9 mm (a2) of Mn70Fe30 (a1, a2), Mn70Fe30 Ti20 (b1, b2), Mn70Fe30_Zr20 (c1, c2) and Mn70Fe30_Ce20 (d1, d2) particle surface: untreated (1) and after thermal cyclization (2)

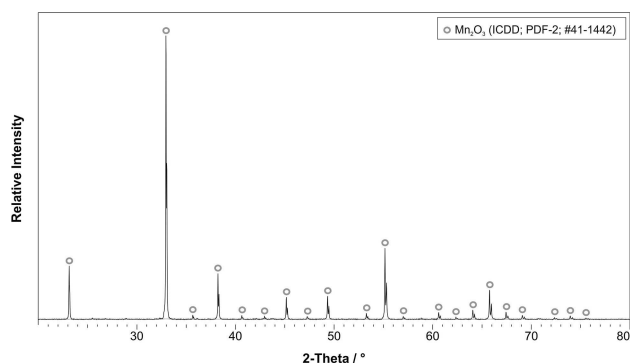


Figure 8. XRD pattern of the manganese-iron-oxide sample after thermal cyclization. Mn_2O_3 (space group: $la3$) can be detected. This pattern overlaps with the Fe_2O_3 pattern (ICDD; PDF-2; #39-0238) (space group: $la3$), so that pure Mn_2O_3 , pure Fe_2O_3 , or $(\text{Mn,Fe})_2\text{O}_3$ cannot be distinguished.

reaction over temperature variation, instead of oxygen pressure variation, chemical and thermal stresses cannot be separated completely. For this reason, additional “temperature shock” experiments were performed.

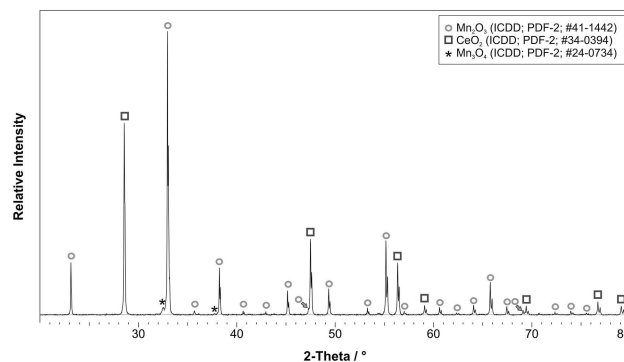


Figure 9. XRD pattern of the manganese-iron-oxide sample with the addition of CeO_2 after thermal cyclization. Mn_2O_3 (space group: $la3$), CeO_2 (space group: $\text{Fm}3m$), and Mn_3O_4 (space group: $I41/amd$) can be detected. As described in Figure 8 overlap with the Fe_2O_3 pattern (ICDD; PDF-2; #39-0238) (space group: $la3$) is possible, so that pure Mn_2O_3 , pure Fe_2O_3 , or $(\text{Mn,Fe})_2\text{O}_3$ cannot be distinguished.

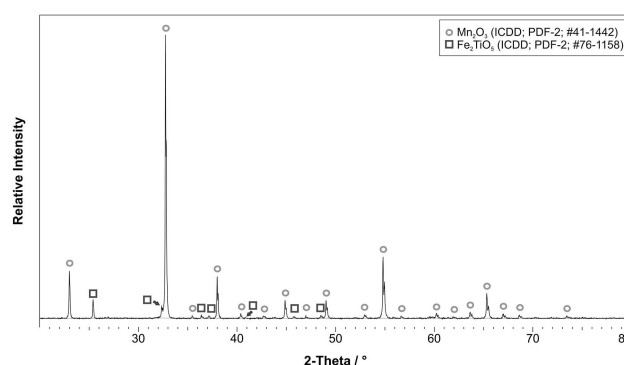


Figure 10. XRD pattern of the manganese-iron-oxide sample with the addition of TiO_2 after thermal cyclization. Mn_2O_3 (space group: $la3$) and Fe_2TiO_5 (space group: $\text{Cm}cn$) can be detected. As described in Figure 8 overlap with the Fe_2O_3 pattern (ICDD; PDF-2; #39-0238) (space group: $la3$) is possible, so that pure Mn_2O_3 , pure Fe_2O_3 , or a $(\text{Mn,Fe})_2\text{O}_3$ cannot be distinguished.

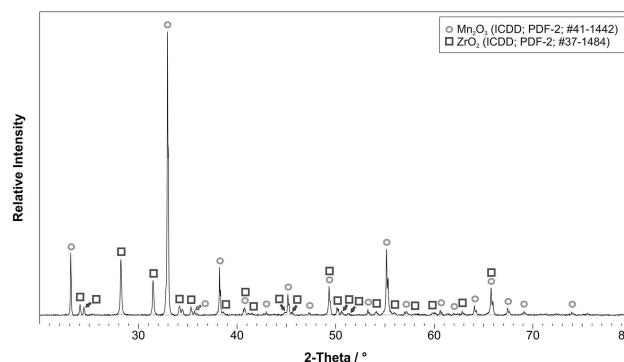


Figure 11. XRD pattern of the manganese-iron-oxide sample with the addition of ZrO_2 after 30 temperature cycles. Mn_2O_3 (space group: $la3$) and ZrO_2 (space group: $\text{P}21/a$) can be detected. As described in Figure 8 overlap with the Fe_2O_3 pattern (ICDD; PDF-2; #39-0238) (space group: $la3$) is possible, so that pure Mn_2O_3 , pure Fe_2O_3 , or a $(\text{Mn,Fe})_2\text{O}_3$ cannot be distinguished.

Effect of Temperature Shocks

The effect of thermal strain on Mn70Fe30, Mn70Fe30_Ce20, and Mn70Fe30_Zr20 samples was investigated by applying high cooling rates to the packed bed. Fifteen subsequent cycles in air and in N₂ were performed. Since Mn70Fe30_Ti20 showed no stable redox reaction in the previous cyclization test, it was excluded from further examination. A nitrogen atmosphere prohibits the re-oxidation of previously reduced manganese-iron oxide particles, whereas an air atmosphere allows a re-oxidation reaction. It must be noted that due to the fast average cooling rate of $110 \pm 4 \text{ K min}^{-1}$, a complete conversion was not reached in air. In general, conversion decreased with cycle number for all samples. While a conversion of 77.7% for reduction and 76.9% for oxidation of Mn70Fe30 was achieved in the first cycle, the conversion dropped to 26.9% for reduction and 31.1% for oxidation in the 15th cycle. Mn70Fe30_Ce20 and Mn70Fe30_Zr20 indicated a similar behavior with a decrease of oxidation conversion of 64.4% to 21.2% and 48.8% to 5.1% respectively.

However, a direct comparison with the experiments performed in N₂ showed clear effects that could be ascribed to the chemical reaction. The differential particle size distribution after a temperature shock test in air atmosphere showed an agglomeration of Mn70Fe30_Ce20 and, especially, Mn70Fe30 particles (Figure 12a). In contrast, thermal strain seemed to provoke splitting of Mn70Fe30_Zr20 particles to nearly half the original diameter.

The particle size distribution for Mn70Fe30_Ce20 and Mn70Fe30 showed no direct splitting effect when the air atmosphere allowed a redox reaction. In contrast, the temperature shock test in the nitrogen atmosphere (Figure 12b) did not initiate any agglomeration of any of the tested compositions. This means that the agglomeration of (Mn_{0.7}Fe_{0.3})₂O₃/(Mn_{0.7}Fe_{0.3})₃O₄-based compositions is strongly related to the phase change caused by the redox reaction in the oxygen atmosphere and was not influenced by heating or cooling rates up to 110 K min^{-1} . An apparent higher splitting of the Mn70Fe30_Zr20 sample in the nitrogen atmosphere than in the air atmosphere could be caused by a stronger reduced phase or experimental variance in sieving due to a rather low mass of 10 to 12 g of sample. However, Mn70Fe30_Ce20 and Mn70Fe30_Zr20 developed higher particle splitting due to thermal stress than Mn70Fe30 particles (Figure 12b). It can be speculated that there could be a superposition of splitting and subsequent agglomeration process for Mn70Fe30_Ce20 because Mn70Fe30_Ce20 indicated minor particle splitting during the temperature shock test in the nitrogen atmosphere but no particle splitting when the air atmosphere allowed for a redox reaction. In the end, the chemical reaction seemed to provoke the agglomeration of unsupported manganese-iron-oxide, and thermal gradients induced the splitting of ZrO₂-supported manganese-iron-oxide particles.

The morphology on the particle surface especially of Mn70Fe30 and Mn70Fe30O_Ce20 changed with the 15 temperature shocks in air or nitrogen (Figure 13 a1–b2). An EDX analysis of Mn70Fe30 after 15 temperature shocks in air

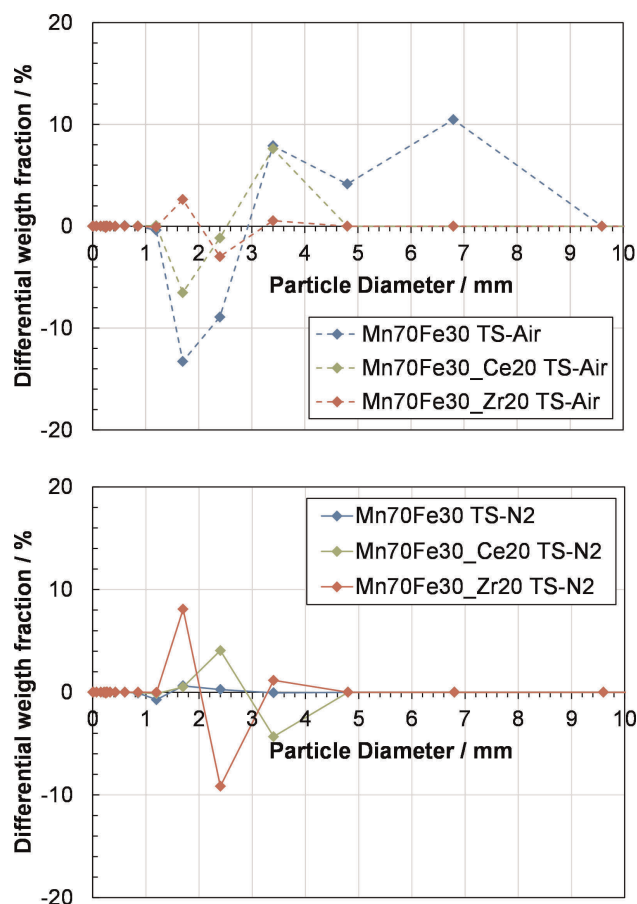


Figure 12. Differential particle size distribution after 15 temperature shocks in air (TS-Air) (a) and nitrogen atmospheres (TS-N2) (b) with Mn70Fe30, Mn70Fe30_Ce20, and Mn70Fe30_Zr20 in a packed bed reactor.

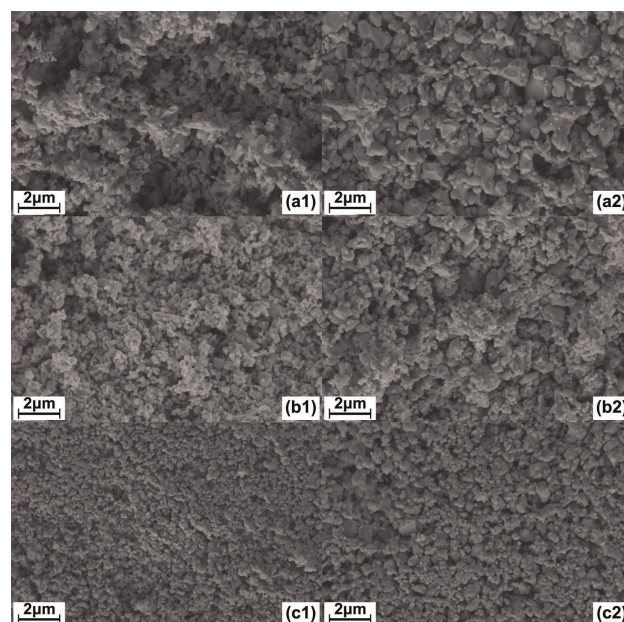


Figure 13. SEM images with 5.0 kV acceleration voltage and working distances 8.0 mm (a1, a2, b1, c1, c2) and 8.1 mm (b2) of Mn70Fe30 (a1, a2), Mn70Fe30_Ce20 (b1, b2) and Mn70Fe30_Zr20 (c1, c2) particle surface: after 15 temperature shock in air (1) or in nitrogen (2)

indicated Mn-rich areas as well as areas with an equal distribution of Mn and Fe cations. Whereas an even cation distribution was detected at the EDX measuring points of Mn70Fe30 after 15 temperature shocks in nitrogen. EDX analysis of Mn70Fe30_Zr20 after the temperature shock test in nitrogen revealed an irregular distribution of Mn, Fe, and Zr cations at the measuring points, whereas the EDX measuring points indicated an equal cation distribution in Mn70Fe30_Zr20 after the temperature shock test in air. However, optically, the surface morphology of Mn70Fe30_Zr20 seems to be the most stable one compared to the other compositions after all experiments (Figure 7 c1–c2 and Figure 13 c1–c2). Detailed EDX data can be found as supporting information.

Particle Stability Investigation

An attrition jet cup was utilized to estimate the tendency towards abrasion of all four compositions in untreated form and after the experiments above. The device was designed for quick screening tests with a low sample weight of 5 g. The mechanical stress in this attrition jet cup is much greater than the stress found under moving bed conditions but may give an indication of the mechanical properties of the sample. The particle size distribution before and after an attrition rig test showed, that the test rig caused both abrasion and fragmentation. Previous examinations of oxygen carriers in the attrition jet cup indicated that the fine production follows either a linear trend over time or a logarithmic trend with a stabilized attrition rate after around 30 min.^[54] Therefore, a total attrition A_{tot} (eq. 2 in Experimental Section) and the attrition rate A_i (eq. 3 in Experimental Section) are used to describe the attrition behavior. The attrition rate corresponds to the slope of the attrition curve over time between 30 min and 1 h operation. The total attrition A_{tot} and the attrition rate A_i in Figure 14 clearly demonstrate the improved attrition behavior of processed material with the addition of ZrO_2 and CeO_2 .

Mn70Fe30_Zr20 promised high particle stability. In comparison to untreated particles, thermal stress, induced with temperature shock test in air or nitrogen, had only a minor effect on particle stability according to the attrition test

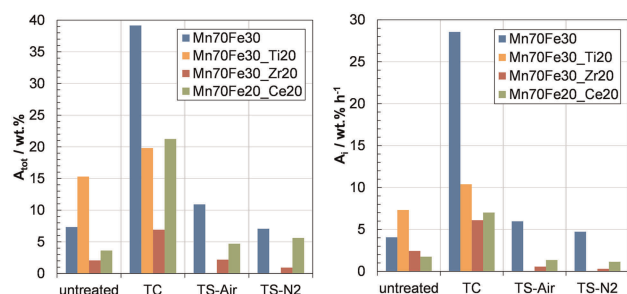


Figure 14. The total attrition (a) and the slope of the attrition curve of the last 30 min (b) of 1 h operation in the attrition jet cup of untreated particles and processed in thermal cyclization (TC) or temperature shock (TS) in air or nitrogen.

method. Fifteen temperature shocks even improved the attrition resistance of Mn70Fe30_Zr20 (Figure 14b). In contrast, 30 temperature cycles increased the total attrition and attrition slope of all material compositions, especially of the unsupported manganese-iron oxide samples. Again, ZrO_2 was found to be the most promising supportive material regarding attrition resistance. However, the attrition rate after thermal cyclization tests with Mn70Fe30_Ce20 is in the range of the Mn70Fe30_Zr20 sample (Figure 14b). In ceramic research, ZrO_2 is known to significantly improve the toughness of alumina due to its high fracture toughness, which describes the resistance of a material to the propagation of preexisting flaws.^[60,61]

The attrition values over time are displayed in Figure 15 with silica sand as a reference material. The Mn70Fe30

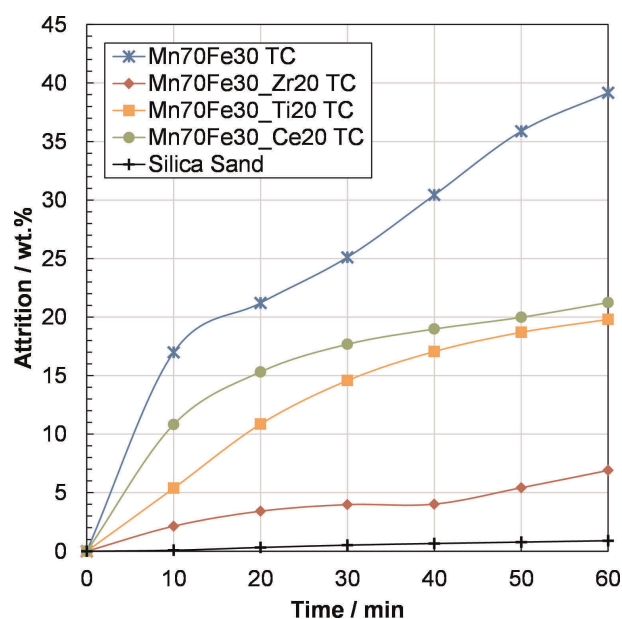


Figure 15. Attrition test of manganese-iron-oxide samples after thermal cyclization. Silica sand is the reference.

sample indicates a linear attrition rate, while the logarithmic attrition curves of Mn70Fe30_Ce20 and Mn70Fe30_Ti20 reach a stable but high level in the figure.

The strong agglomeration tendency and low particle stability (abrasion and disintegration) of Mn70Fe30, which is mainly caused by the chemical stress, can be ameliorated by supporting the manganese-iron oxide with ZrO_2 or CeO_2 . From a technical point of view, the choice of modified material depends mainly on the mechanical and thermal stress the particles will experience in the chosen reactor and process concept. In applied reactor concepts, which cause high mechanical stress, e.g. a fluidized bed reactor, Mn70Fe30_Zr20 is the favored composition of the investigated materials in this paper. The attrition test and the 30 temperature cycles proved strong particle stability. However, in comparison to the other compositions, Mn70Fe30_Zr20 indicated a tendency to particle splitting when high temperature gradients oc-

curred. Considering reactor or process concepts with lower attrition risk, e.g. a packed bed, Mn₇₀Fe₃₀-Ce₂₀ showed advantages over Mn₇₀Fe₃₀-Zr₂₀ particles since it reached the highest oxidation conversion of all the modified particles. Even though Mn₇₀Fe₃₀-Ce₂₀ shows the highest attrition in total numbers for the supported manganese-iron oxides, the slope of the attrition curve (tendency for stabilization) is similar to the results found using Mn₇₀Fe₃₀-Zr₂₀ and a major improvement over Mn₇₀Fe₃₀ particles. In conclusion, supporting Mn₇₀Fe₃₀ with ZrO₂ or CeO₂ promises a prolonged mechanical particle lifetime. However, it must be noted that the production process influences the overall stability behavior of the particles. In future research, an optimal ratio of active manganese-iron-oxide particles to inert ZrO₂ or CeO₂ content will be addressed in terms of particle stability, agglomeration tendency, and reaction conversion.

Conclusions

The reactivity and particle stability of (Mn_{0.7}Fe_{0.3})₂O₃ as an active material supported by 20 wt.% of either CeO₂, ZrO₂, or TiO₂ was tested in a packed bed reactor and with an attrition test rig. From a technical engineering standpoint, the following conclusions can be drawn:

- Mn-Fe oxides are very well suited as thermochemical storage material and oxygen carrier material for chemical-looping combustion.
- Pure (Mn_{0.7}Fe_{0.3})₂O₃ showed the highest reactivity and redox conversion. However, it also showed a great tendency towards agglomeration and low particle stability, which reduces the expected lifetime of the particle. Therefore, a modification of this material is mandatory, despite the drawback of reduced energy density.
- The addition of TiO₂ led to a deactivation of the manganese-iron oxide by forming pseudobrookite.
- Pure (Mn_{0.7}Fe_{0.3})₂O₃ and (Mn_{0.7}Fe_{0.3})₂O₃ supported with CeO₂ or ZrO₂ showed sufficient cycle stability. The reaction rate was faster with the addition of CeO₂ than with ZrO₂ under the experimental conditions, but was still slower than with pure (Mn_{0.7}Fe_{0.3})₂O₃. Consequently, the operational conditions must be adjusted (e.g. a longer reaction time) to avoid incomplete conversion.
- All investigated additives hindered or clearly decreased the agglomeration and improved the particle strength of manganese-iron-oxide particles. Especially ZrO₂ promises a higher resistance towards attrition. A variation of the CeO₂ or ZrO₂ content should be addressed in future research to optimize the particle from the attrition, agglomeration, and reaction rate standpoints for use as thermochemical storage material or oxygen carrier.

Experimental Section

Materials Preparation

The Flemish Institute for Technological Research (VITO) in Belgium produced the particles with a build-up granulation technique by mixing the raw materials Mn₃O₄ (Chemalloy, Triminox), Fe₂O₃ (Alfa Aesar, 99 %) and one of the supports TiO₂ (Venator, Hombikat™ M211), CeO₂ (American Elements, 99 %) or ZrO₂ (Saint Gobain, 99.9 % ZrO₂ + HfO₂). A pretreatment in air at 800 °C for 10 h allowed Mn₃O₄ and Fe₂O₃ to change into the bixbyite (Mn,Fe)₂O₃ phase. After granulation, the particles were sieved to a size between 2 and 3 mm.

Materials Characterization

The weight loss due to reduction was measured with a simultaneous thermal analyzer from Netzsch (STA 449 F3 Jupiter®) to confirm equation (1). Two particles with a total mass of 30 mg were oxidized at 850 °C for 5 h in a Pt/Rh crucible without a cap in an atmosphere containing 20 % oxygen (Linde, 99.995 %) and 80 % nitrogen (Linde, 99.999 %). The reduction was initiated by increasing the temperature with a heating rate of 20 K min⁻¹ up to 1050 °C in a nitrogen atmosphere and maintaining the temperature for 5 h. A total gas flow of 100 ml min⁻¹ was kept constant for the entire test.

An analysis of crystalline phases of manganese-iron-oxide particles was performed with an X-ray diffractometer (Bruker D8 Advance with Cu-Kα_{1,2} radiation). Scanning electron microscopy (Zeiss Ultra 55) gave information about the shape and morphology of the particles and their polished microsection in combination with energy dispersive X-ray point measurements (Oxford Inca Penta FETX3). EDX measurements were performed with the secondary electron detector at a working distance of 8 mm with accelerating voltage of 15.0 kV and are listed as supporting information. Oxygen has been detected with EDX but is not listed in the supporting information, due to inaccuracy of the EDX measuring method in case of oxygen.

The bulk density was measured by filling and weighing a 50 ml glass cylinder with 2–3 mm particles.

A customized jet cup is available at Chalmers University of Technology in Gothenburg, Sweden, to evaluate the attrition resistance of the oxygen carriers used for chemical looping combustion. A detailed description of the attrition rig setup can be found in.^[54] A sample mass of 5 g was fit into an attrition cup and was fluidized with a moisturized air flow entering the cup through a nozzle. The particles were fluidized into a settling chamber above the cup. A minimal gas flow of 16 Nl min⁻¹ carried fines with a diameter below 10 μm through the settling chamber to a particle filter at the top of the chamber, since the terminal velocity of the densest particles equals the gas velocity in the widest part of the settling chamber. The change of filter weight at the gas exit corresponded to the fine production during the measuring time. The total fine production A_{tot} caused by attrition for a measuring period of 1 h was calculated according to equation (2).

$$A_{\text{tot}} = 100 \cdot \frac{m_{f,1h} - m_{f,\text{start}}}{m_s} \quad (\text{wt.}\%) \quad (2)$$

The attrition rate describes the trend of the attrition curve between 30 min and 1 h operation and is calculated according to equation (3).

$$A_i = 100 * \frac{60}{30} * \frac{m_{f,1h} - m_{f,30\min}}{m_s} \text{ (wt.\% h}^{-1}\text{)} \quad (3)$$

In equations (2) and (3), m_s is the sample weight placed in the cup and $m_{f,t}$ equals the filter weight for a given operation time t .

Experiments in a Packed Bed Reactor

Thermal cyclization tests and temperature shock tests were performed in a packed bed reactor. Particles were placed on a porous quartz plate in a glass tube, and gas was introduced at the bottom of the reactor (Figure 16). A detailed description of the reactor setup can be found in.^[51]

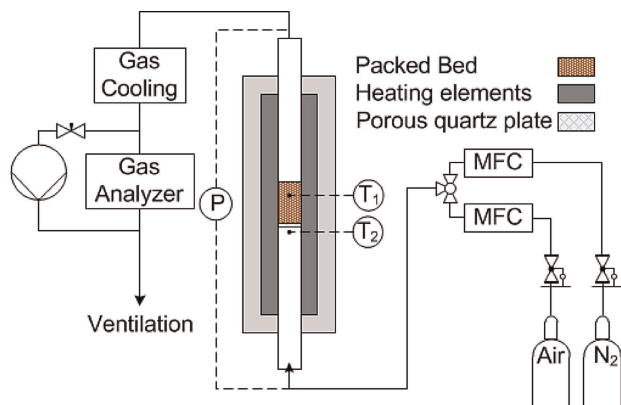


Figure 16. Schematic setup of the packed bed reactor.

The set temperature for the oven was controlled by two thermocouples (Pentronic CrAl/NiAl with inconel-600), each enclosed in a quartz thermowell. One was placed 25 mm above the quartz plate (T_1), and one was placed 5 mm below the plate (T_2). The bed height always exceeded 25 mm and thermocouple T_1 was employed to determine the bed temperature. The reactor could be used as a packed bed or fluidized bed depending on gas velocity. A gas flow of 3 Nl min^{-1} was chosen for all experiments, which resulted in a packed bed operation since the flow was well below the minimum fluidization velocity.

Thermal cyclization was conducted by varying the temperature with a heating rate of 20 K min^{-1} between 850°C for oxidation and 1050°C for reduction in the packed bed reactor. The redox reaction was initiated by changing the temperature. An isothermal step followed each heating and cooling phase for 12 min at 1050°C and for 6 min at 850°C . 30 redox cycles were performed with a mass of 21 g manganese-iron oxide material or 26 g supported manganese-iron oxide material to compensate for the possibly inert additive. The thermal cyclization experiments were executed on two consecutive days, and the packed bed reactor was cooled to ambient temperature in air at the end of the first day.

The fast cooling rates for the temperature shock tests were achieved by opening the oven circa 4 cm to permit effective cooling rates of $110 \pm 4 \text{ K min}^{-1}$. A sample of 10 g manganese-iron-oxide particles or 12 g manganese-iron-oxide with an additive was placed on the quartz plate for temperature shock test. The temperature shock tests were performed 15 times in air for an oxidizing environment and 15 times in a pure nitrogen atmosphere for a reducing environment.

Acknowledgements

The authors acknowledge the work of the late Dongmei Zhao (deceased Dec. 18, 2016). At the time of her death, she was deeply involved in this research and made many important contributions. Financial support was provided by DLR internal funding and ÅForsk.

Conflict of Interest

The authors declare no conflict of interest.

Keywords: Manganese · Iron · Redox chemistry · Thermochemistry · Particle stability

- [1] A. Lyngfelt, B. Leckner, T. Mattisson, *Chem. Eng. Sci.* **2001**, 56, 3101–3113
- [2] T. Mattisson, A. Lyngfelt, H. Leion, *Int. J. Greenhouse Gas Control* **2009**, 3, 11–19
- [3] A. Abad, I. Adánez-Rubio, P. Gayán, F. García-Labiano, L. F. de Diego, J. Adánez, *Int. J. Greenhouse Gas Control* **2002**, 6, 189–200
- [4] L. Xu, H. Sun, Z. Li, N. Cai, *Appl. Energy* **2016**, 162, 940–947
- [5] A. Lyngfelt, C. Linderholm, *Energy Procedia* **2014**, 63, 98–112
- [6] J. Ströhle, M. Orth, B. Epple, *Appl. Energy* **2015**, 157, 288–294
- [7] M. Arjmand, A. Hedayati, A.-M. Azad, H. Leion, M. Rydén, T. Mattisson, *Energy Fuels* **2013**, 27, 4097–4107
- [8] N. M. Pour, G. Azimi, H. Leion, M. Rydén, T. Mattisson, A. Lyngfelt, *Energy Technol.* **2014**, 2, 469–479
- [9] M. Arjmand, H. Leion, A. Lyngfelt, T. Mattisson, *Int. J. Greenhouse Gas Control* **2012**, 8, 56–60
- [10] A. Steinfeld, *Sol. Energy* **2005**, 78, 603–615
- [11] D. Marxer, P. Furler, M. Takacs, A. Steinfeld, *Energy Environ. Sci.* **2017**, 10, 1142–1149
- [12] L. O. Schunk, P. Haeberling, S. Wepf, D. Wüillemin, A. Meier, A. Steinfeld, *J. Sol. Energy Eng.* **2008**, 130, 021009
- [13] N. Gokon, T. Mataga, N. Kondo, T. Kodama, *Int. J. Hydrogen Energy* **2011**, 36, 4757–4767
- [14] S. Abanades, P. Charvin, G. Flamant, *Chem. Eng. Sci.* **2007**, 62, 6323–6333
- [15] R. B. Diver, J. E. Miller, M. D. Allendorf, N. P. Siegel, R. E. Hogan, *J. Sol. Energy Eng.* **2008**, 130, 041001–041001-8
- [16] I. Ermanoski, N. P. Siegel, E. B. Stechel, *J. Sol. Energy Eng.* **2013**, 135, 031002–031002-10
- [17] E. Koepf, S. G. Advani, A. Steinfeld, A. K. Prasad, *Int. J. Hydrogen Energy* **2012**, 37, 16871–16887
- [18] P. Lichty, X. Liang, C. Muhich, B. Evanko, C. Bingham, A. W. Weimer, *Int. J. Hydrogen Energy* **2012**, 37, 16888–16894
- [19] L. J. Venstrom, R. M. De Smith, Y. Hao, S. M. Haile, J. H. Davidson, *Energy Fuels* **2014**, 28, 2732–2742
- [20] S. Abanades, H. I. Villafan-Vidales, *Chem. Eng. J.* **2011**, 175, 368–375
- [21] C. Agrafiotis, M. Roeb, M. Schmücker, C. Sattler, *Sol. Energy* **2014**, 102, 189–211.
- [22] T. Block, M. Schmücker, *Sol. Energy* **2016**, 126, 195–207
- [23] A. J. Carrillo, J. Moya, A. Bayón, P. Jana, V. a. de la Peña O'Shea, M. Romero, J. Gonzalez-Aguilar, D. P. Serrano, P. Pizarro, J. M. Coronado, *Sol. Energy Mater. Sol. Cells* **2014**, 123, 47–57
- [24] W. E. Wentworth, E. Chen, *Sol. Energy* **1976**, 18, 205–214.
- [25] C. Prieto, P. Cooper, A. I. Fernández, *Renewable Sustainable Energy Rev.* **2016**, 60, 909–929
- [26] H. Zhang, J. Baeyens, G. Cáceres, J. Degrève, Y. Lv, *Prog. Energy Combust. Sci.* **2016**, 53, 1–40
- [27] M. Romero, A. Steinfeld, *Energy Environ. Sci.* **2012**, 5, 9234–9245
- [28] A. J. Schrader, A. P. Muroyama, P. G. Loutzenhiser, *Sol. Energy* **2015**, 118, 485–495

- [29] E. Alonso, C. Pérez-Rábago, J. Licurgo, E. Fuentealba, C. A. Estrada, *Sol. Energy* **2015**, *115*, 297–305
- [30] M. Neises, S. Tescari, L. de Oliveira, M. Roeb, C. Sattler, B. Wong, *Sol. Energy* **2012**, *86*, 3040–3048
- [31] A. S. Oles, G. S. Jackson, *Sol. Energy* **2015**, *122*, 126–147
- [32] A. J. Schrader, G. De Dominicis, G. L. Schieber, P. G. Loutzenhiser, *Sol. Energy* **2017**, *150*, 584–595
- [33] E. Alonso, F. Gomez-Garcia, J. Gozalez-Aguilar, M. Romero, *Proceedings of the SolarPACES Conference, Spain* **2011**, 20–23.
- [34] M. Wokon, A. Kohzer, M. Linder, *Sol. Energy* **2017**, *153*, 200–214
- [35] S. Álvarez de Miguel, J. Gonzalez-Aguilar, M. Romero, *Energy Procedia* **2014**, *49*, 676–683
- [36] J. V. Crum, B. J. Riley, J. D. Vienna, *J. Am. Ceram. Soc.* **2009**, *92*, 2378–2384
- [37] L. Kjellqvist, M. Selleby, *J. Phase Equilib. Diffus.* **2010**, *31*, 113–134
- [38] A. Muan, S. Sōmiya, *Am. J. Sci.* **1962**, *260*, 230–240
- [39] D. G. Wickham, *J. Inorg. Nucl. Chem.* **1969**, *31*, 313–320
- [40] L. André, S. Abanades, L. Cassayre, *J. Solid State Chem.* **2017**, *253*, 5–14
- [41] A. Carrillo, D. P. Serrano, P. Pizarro, J. M. Coronado, *ChemSusChem* **2015**, *8*, 1947–1954
- [42] M. Wokon, T. Block, S. Nicolai, M. Linder, M. Schmücker, *Sol. Energy* **2017**, *153*, 471–485
- [43] G. Azimi, H. Leion, M. Ryden, T. Mattisson, A. Lyngfelt, *Energy Fuels* **2013**, *27*, 367–377
- [44] C. H. Bartholomew, *Appl. Catal. A* **2001**, *212*, 17–60
- [45] Y. Zhong, Z. Wang, Z. Guo, Q. Tang, *Powder Technol.* **2014**, *256*, 13–19
- [46] T. A. Brown, F. Scala, S. A. Scott, J. S. Dennis, P. Salatino, *Chem. Eng. Sci.* **2012**, *71*, 449–467
- [47] C. R. Bemrose, J. Bridgwater, *Powder Technol.* **1987**, *49*, 97–126
- [48] S. Bhavsar, B. Tackett, G. Veser, *Fuel* **2014**, *136*, 268–279
- [49] A. Khadilkar, P. L. Rozelle, S. V. Pisupati, *Powder Technol.* **2014**, *264*, 216–228
- [50] Y. De Vos, M. Jacobs, P. Van Der Voort, I. Van Driessche, F. Snijckers, A. Verberckmoes, *Chem. Eng. J.* **2017**, *309*, 824–839
- [51] G. Azimi, H. Leion, T. Mattisson, M. Ryden, F. Snijckers, A. Lyngfelt, *Ind. Eng. Chem. Res.* **2014**, *53*, 10358–10365
- [52] M. Abián, A. Abad, M. T. Izquierdo, P. Gayán, L. F. de Diego, F. García-Labiano, J. Adánez, *Fuel* **2017**, *195*, 38–48
- [53] M. Jacobs, J. Van Noyen, Y. Larring, M. Mccann, M. Pishahang, S. Amini, M. Ortiz, F. Galluci, M. V. Sint-Annaland, D. Tournigant, E. Louradour, F. Snijckers, *Appl. Energy* **2015**, *157*, 374–381
- [54] M. Rydén, P. Moldenhauer, S. Lindqvist, T. Mattisson, A. Lyngfelt, *Powder Technol.* **2014**, *256*, 75–86
- [55] A. Tilland, J. Prieto, D. Petitjean, E. Schaer, *Chem. Eng. J.* **2016**, *302*, 619–632
- [56] I. Barin in *Thermochemical data of pure substances*, Vol. 3 (Eds.: K. Sora, J. Gardiner), VCH Verlagsgesellschaft mbH, Weinheim, **1995**.
- [57] A. Cabello, P. Gayán, F. García-Labiano, L. F. de Diego, A. Abad, J. Adánez, *Fuel Process. Technol.* **2016**, *148*, 188–197
- [58] F. Scala, F. Montagnaro, P. Salatino, *Energy Fuels* **2007**, *21*, 2566–2572
- [59] B. Amblard, S. Bertholin, C. Bobin, T. Gauthier, *Powder Technol.* **2015**, *274*, 455–465
- [60] N. Claussen, *J. Am. Ceram. Soc.* **1976**, *59*, 49–51
- [61] S. Hori, M. Yoshimura, S. Sōmiya, *J. Mater. Sci. Lett.* **1985**, *4*, 413–416
- [62] L. M. Anovitz, A. H. Treiman, E. J. Essene, B. S. Hemingway, E. F. Westrum Jr., V. J. Wall, R. Burriel, S. R. Bohlen in *The Heat-capacity of ilmenite and phase equilibria in the system Fe-Ti-O*, *Geochimica et Cosmochimica Acta* **49**, Pergamon Press Ltd., **1985**, pp. 2027–2040.

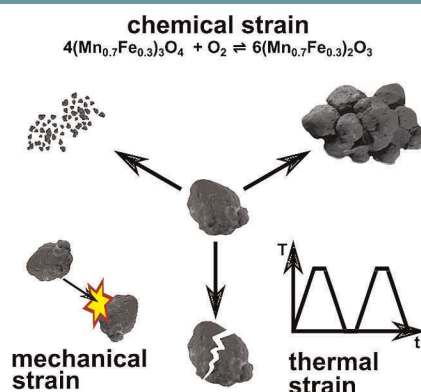
Manuscript received: ■■■, ■■■■

Accepted Article published: April 25, 2018

Version of record online: April 26, 2018

FULL PAPER

Particle degeneration and agglomeration is one challenge for an application of metal oxides in the discipline of thermochemical storage and chemical-looping combustion. By supporting manganese-iron oxide granules with additives, such as e.g. ZrO_2 or CeO_2 , the tendency towards agglomeration and attrition can be minimized tremendously.



N. C. Preisner, Dr. T. Block,
Dr. M. Linder, Dr. H. Leion*

1 – 13

Stabilizing Particles of Manganese-iron Oxide with Additives for Thermochemical Energy Storage



SPACE RESERVED FOR IMAGE AND LINK

Share your work on social media! *Energy Technology* has added Twitter as a means to promote your article. Twitter is an online microblogging service that enables its users to send and read short messages and media, known as tweets. Please check the pre-written tweet in the galley proofs for accuracy. If you, your team, or institution have a Twitter account, please include its handle @username. Please use hashtags only for the most important keywords, such as #catalysis, #nanoparticles, or #proteindesign. The ToC picture and a link to your article will be added automatically, so the **tweet text must not exceed 250 characters**. This tweet will be posted on the journal's Twitter account (follow us @EnergyTechnology) upon publication of your article in its final (possibly unpaginated) form. We recommend you to re-tweet it to alert more researchers about your publication, or to point it out to your institution's social media team.

ORCID (Open Researcher and Contributor ID)

Please check that the ORCID identifiers listed below are correct. We encourage all authors to provide an ORCID identifier for each coauthor. ORCID is a registry that provides researchers with a unique digital identifier. Some funding agencies recommend or even require the inclusion of ORCID IDs in all published articles, and authors should consult their funding agency guidelines for details. Registration is easy and free; for further information, see <http://orcid.org/>.

N. C. Preisner
Dr. T. Block
Dr. M. Linder
Dr. H. Leion